

PROCEEDINGS  
OF THE  
ROYAL IRISH ACADEMY  
PAPERS READ BEFORE THE ACADEMY



ZONAL INFLUENCES IN A MODIFIED STOMMEL–ARONS MODEL OF  
THE ABYSSAL OCEAN CIRCULATION

By P.F. HODNETT\* R. MCNAMARA  
Department of Mathematics and Statistics, University of Limerick

[Received 8 May 2000. Read 13 November 2000. Published 30 August 2002.]

ABSTRACT

The Stommel–Arons model of the circulation in the abyssal ocean is modified by allowing the temperature (homogeneous in Stommel–Arons) to vary with depth and latitude and weakly with longitude. The temperature and vertical velocity are specified at the top of the abyss as functions of latitude and weakly of longitude. The resulting distributions of temperature for the North Atlantic show agreement with climatological data when the vertical coefficient of thermal diffusion is  $1.25 \times 10^{-4} \text{ m}^2 \text{ s}^{-1}$ . The vertical, meridional and zonal components of velocity show significant change in structure from the Stommel–Arons expressions. Also the resulting streamline pictures are significantly different from the Stommel–Arons solution. The simple model of the abyssal ocean presented here yields results consistent with some specific observations and with some aspects of three-dimensional numerical models of the North Atlantic circulation which more fully represent the physical reality.

**1 Introduction**

Until the relatively recent past the understanding of the abyssal ocean circulation resided in the simple model presented by Stommel and Arons ([12]; [13]). In this model the temperature is assumed to be homogeneous throughout the entire abyss. In their uniform case the resulting meridional (as well as vertical) component of velocity is independent of longitude, with only the zonal component of velocity depending on longitude. The vertical velocity varies linearly from zero at the (flat) ocean bottom to the top of the abyss (or base of the thermocline region). In the North Atlantic this upwelling from the abyssal region is fed from a southward-flowing western boundary current whose source is a downwelling point at the

---

\*Corresponding author, e-mail: Frank.Hodnett@ul.ie

northern extremity of the basin. In the North Pacific the upwelling is also fed from a western boundary current whose source is outside the ocean basin at a downwelling point in the Weddell Sea. From the Weddell Sea downwelling point a western boundary current flows northward in the South Pacific to cross the equator into the North Pacific and proceeds towards a stagnation point (in the western boundary current) north of which the flow is southward.

More recently Pedlosky ([9]) considered the baroclinic structure of the abyssal circulation by allowing the temperature to vary with position in the abyss. However, he assumed a particular form for the temperature field where the primary variation is in the vertical modified by a small perturbation which varies with depth, latitude and longitude. The resulting equation for the temperature is linear. This linear model of the thermodynamics was first introduced by Lineykin ([7]) and later used by Pedlosky ([8]) and Gill ([3]) to study the linearised thermocline equations. The weakness of the model is that (contrary to the model assumption) lateral variations of temperature are not much smaller than vertical variations in the abyss. In addition, Pedlosky ([9]) assumes that the upwelling through the top of the abyss is non-uniform but varies with longitude by decreasing continuously towards the west from a maximum at the eastern boundary. This assumption is consistent with theoretical predictions that the upwelling is more intense in the eastern part of the ocean where the thermocline vertical scale is least. His model gives a meridional velocity which changes sign with depth in the western ocean, agreeing with observations from which it can be deduced that Antarctic Bottom water flows north beneath North Atlantic Deep water flowing south beneath Antarctic Intermediate water flowing north, all beneath the thermocline.

A different approach is adopted by Hodnett and McNamara ([4]) in allowing the temperature to vary with depth and latitude and in assuming that the variation with longitude is negligible. The assumption that longitudinal variations in temperature are negligible is based on a consideration of climatological data in [6, fig. 16, p. 122] showing annual mean potential temperature ( $^{\circ}\text{C}$ ) at 1500m depth where weaker longitudinal than meridional variations in temperature are seen in both the North Atlantic and North Pacific (especially in the North Pacific). Hodnett and McNamara ([4]) allow the temperature and vertical velocity at the top of the abyss to vary with latitude (not with longitude) to test how these changes modify the Stommel and Arons ([12]; [13]) abyssal circulation. They also distinguish between the North Pacific and North Atlantic oceans since the data in [6] show distinguishably different annual mean temperature fields at 1500m depth ([6, fig. 16, p. 122]) and at the bottom of the ocean, i.e. 4000m depth ([6, fig. 21, p. 124]), where the North Pacific is colder at approximately  $1.15^{\circ}$  than the North Atlantic at approximately  $2.0^{\circ}\text{C}$ .

The model in [4] emphasises the substantial changes which occur in the Stommel–Arons model of the abyssal circulation when that model is altered by allowing temperature to vary with depth and latitude, and yields results consistent with some observations in [14] and with some aspects of the three-dimensional numerical model of the North Atlantic circulation given in [1].

Here we allow for *weak* zonal variation in temperature which was neglected in [4] and identify the substantial resulting changes in the vertical and meridional velocity components. The results produced are also compared with some results from [9].

## 2 Equations and boundary conditions

The equations which describe steady motion in the abyss (and thermocline region) are the planetary geostrophic equations, which in non-dimensional form are

$$\frac{\partial p}{\partial z} = T, \quad 2u \sin \phi = -\frac{\partial p}{\partial \phi}, \quad 2v \sin \phi = \frac{1}{\cos \phi} \frac{\partial p}{\partial \lambda}, \quad (2.1a,b,c)$$

$$\frac{\partial w}{\partial z} = v / \tan \phi, \quad (2.2)$$

$$w \frac{\partial T}{\partial z} + v \frac{\partial T}{\partial \phi} + \frac{u}{\cos \phi} \frac{\partial T}{\partial \lambda} = \beta \frac{\partial^2 T}{\partial z^2}, \quad (2.3)$$

with thermal diffusion only in the vertical and where (2.2) is the planetary divergence relation which results from substitution of expressions (2.1 b,c) for  $u$  and  $v$  into the continuity equation. In the above equations  $\lambda$  is longitude (positive eastwards),  $\phi$  is latitude (positive northwards),  $z$  is vertical distance (positive upwards),  $p$  is pressure,  $T$  is temperature, and  $u, v, w$  are the respective velocity components in the directions  $\lambda, \phi, z$  increasing. In equation (2.3) it is assumed that horizontal heat diffusion is negligible in comparison with vertical heat diffusion. It was found, through numerical experimentation, that when horizontal heat diffusion is included at the same order as vertical heat diffusion in the non-dimensional equation (2.3) then its influence on the solution is negligible, and on the basis of using the simplest possible model it is set at zero here. For reference the physical variables, denoted by primes, are given as follows:  $(u', v') = U(u, v)$ ,  $w' = Ww$ ,  $z' = Dz$ ,  $k'_z$  (vertical coefficient of heat diffusion) =  $DW\beta$ , and temperature,  $t'$  is given by  $T = (t' - t'_0)/t'_0$ . We take  $W = 2 \times 10^{-7} \text{ m s}^{-1}$  based on the following considerations. Stommel ([11]) took  $W = 3 \times 10^{-7} \text{ m s}^{-1}$ , and later Stommel and Arons ([12]; [13]) suggested that this value is probably too large by a factor of two. An estimate from Yuan *et al.* ([16]) gives  $W = 2.25 \times 10^{-7} \text{ m s}^{-1}$ . In his two-level model for the wind and buoyancy-forced circulation Huang ([5]) derives the upwelling velocity at the top of the abyss (these results were later used in [2]), which varies from  $5 \times 10^{-6} \text{ m s}^{-1}$  at the equator to  $0.01 \times 10^{-6} \text{ m s}^{-1}$  at  $50^\circ \text{ N}$ . His mid-basin values are of order  $2 \times 10^{-7} \text{ m s}^{-1}$ . In the derivation of the above form for the hydrostatic equation it is assumed that the physical density,  $\rho'$ , varies only with temperature in the form  $\rho' = \rho'_0 [1 - \alpha(t' - t'_0)]$  where  $\rho'_0$  is the reference density (taken to be  $10^3 \text{ kg m}^{-3}$ ) and  $\alpha$  is the coefficient of thermal expansion (taken to be  $2 \times 10^{-4} (\text{°C})^{-1}$ ). The pressure  $p'$  is written as  $p' = -\rho'_0 g z' = \bar{p}$  where  $g$  is gravity (taken to be  $9.81 \text{ m s}^{-2}$ ) and  $\bar{p} = (\rho'_0 a \Omega U) p$  where  $a$  is the earth's radius (taken to be  $6.3 \times 10^6 \text{ m}$ ) and  $\Omega$  the earth's rotation rate (taken to be  $0.7 \times 10^{-4} \text{ s}^{-1}$ ). The non-dimensional equations (2.1) to (2.3) result through taking  $(g \alpha t'_0 D) / (a \Omega U) = 1$  and  $U = aW/D$  so that the scale depth,  $D$ , of the abyss and magnitude,  $U$ , of the horizontal speed are given in terms of the magnitude,  $W$ , of the vertical speed by

$$D = \left[ \frac{a^2 \Omega W}{g \alpha t'_0} \right]^{1/2} \quad \text{and} \quad U = \left[ \frac{W g \alpha t'_0}{\Omega} \right]^{1/2}. \quad (2.4)$$

We concentrate here on the North Atlantic basin by taking the reference temperature

at the ocean bottom from [6, fig. 21, p. 124] to be  $t'_0 = 2.0^\circ\text{C}$ . The resulting values for  $D$ ,  $U$  (from equation (2.4)) are:  $D = 376\text{m}$ ;  $U = 3.35 \times 10^{-3} \text{ m s}^{-1}$ . Note that we take the abyss to lie between 1500m depth and 4000m depth so that the bottom of the abyss is at  $z = -\gamma$  where  $D\gamma = 2500\text{m}$ , i.e.  $\gamma = 6.643$ . Pedlosky ([9]) takes the vertical scale of the abyss to be 4000m.

The boundary conditions are as follows:

- (i) there is an assigned temperature distribution and upwelling velocity at the top of the abyss, i.e.

$$T = T_s(\lambda, \phi) \text{ and } w = w_s(\lambda, \phi) \text{ at } z = 0; \quad (2.5)$$

- (ii) temperature is constant and the normal component of velocity is zero at the (flat) ocean floor, i.e.

$$T = 0 \text{ and } w = 0 \text{ at } z = -\gamma. \quad (2.6)$$

An alternative to condition (2.6) for the temperature would be to set the vertical heat flux to zero at the bottom of the abyss. Like Pedlosky ([9]) we take constant temperature at the ocean floor.

It transpires that the velocity field is not able to satisfy a condition of zero normal flow at the eastern boundary (the Stommel–Arons ([12]; [13])) solution does satisfy zero normal flow at the eastern boundary) but is able to satisfy the weaker condition that the integrated (from bottom to top of the abyss) mass transport at the eastern boundary is zero. We therefore impose this weaker boundary condition, i.e.

$$\int_{s=-1}^{s=0} u ds = 0 \text{ at } \lambda = \lambda_E, \quad (2.7)$$

where the vertical coordinate  $z$  is replaced by  $s = z/\gamma$ . Note that  $\lambda = \lambda_E$  (a line of longitude) is the eastern boundary where  $\lambda_E = 5\pi/18$  represents the North Atlantic. The application of this weak eastern boundary condition to the problem assumes the existence of an abyssal eastern boundary layer which is able to accept transport across the eastern boundary. In this eastern boundary layer (not resolved here) viscosity and horizontal heat diffusion (neglected here) are important.

Equations (2.1a,b,c) and (2.2), together with the boundary conditions on  $w$  (at  $s = 0$  and  $s = -1$ ) and the eastern boundary conditions (2.7), give

$$v = \frac{\tan \phi w_s(\lambda, \phi)}{\gamma} + \frac{\gamma}{\sin 2\phi} \left[ \int_{-1}^s \frac{\partial T}{\partial \lambda} ds' - \int_{-1}^0 \int_{-1}^{s'} \frac{\partial T}{\partial \lambda} ds'' ds' \right] \quad (2.8)$$

$$w = (1 + s)w_s(\lambda, \phi) + \frac{\gamma^2}{2\sin^2 \phi} \left[ \int_{-1}^s \int_{-1}^{s'} \frac{\partial T}{\partial \lambda} ds'' ds' - (1 + s) \int_{-1}^0 \int_{-1}^{s'} \frac{\partial T}{\partial \lambda} ds'' ds' \right] \quad (2.9)$$

$$-2u \sin \phi = \gamma \left[ \int_{-1}^s \frac{\partial T}{\partial \phi} ds' - \int_{-1}^0 \int_{-1}^{s'} \frac{\partial T}{\partial \phi} ds'' ds' \right] + \frac{2}{\gamma} \frac{\partial}{\partial \phi} \left[ \sin^2 \phi \int_{\lambda'=\lambda_E}^{\lambda'=\lambda} w_s(\lambda', \phi) d\lambda' \right]. \quad (2.10)$$

The influence of the zonal variation in temperature is seen explicitly (through the terms  $\partial T/\partial\lambda$ ) in the expression for  $v$ ,  $w$  and is also present in the expression for  $u$  since  $T$  varies with  $\lambda$ . When written in terms of  $s = z/\gamma$  equation (2.3) for  $T$  becomes

$$w \frac{\partial T}{\partial s} + \gamma v \frac{\partial T}{\partial \phi} + \frac{\gamma u}{\cos \phi} \frac{\partial T}{\partial \lambda} = \bar{\beta} \frac{\partial^2 T}{\partial s^2} \quad (2.11)$$

where  $\bar{\beta} = \beta/\gamma$ .

Equation (2.11) with expressions (2.8), (2.9), (2.10) is a three-dimensional problem coupling the temperature,  $T$ , with velocity components  $u, v, w$ . Stommel and Arons ([12]; [13]) assumed that temperature is constant, while Hodnett and McNamara ([4]) assumed that  $\partial T/\partial\lambda$  is zero. Here we assume that  $\partial T/\partial\lambda$  is small but non-zero.

### 3 Solution process

To solve this three-dimensional problem we assume that there is *weak* longitudinal variation in temperature characterised by a small but non-zero parameter  $\epsilon$ . When  $\epsilon = 0$  there is no longitudinal variation in temperature and this is the zero-order solution through which, as later described, solution for small, but non-zero,  $\epsilon$  is constructed. In this way the complicated three-dimensional problem coupling velocity and temperature is reduced to a set of linked two-dimensional problems at a set of longitude locations. Such simple models of the ocean have previously been shown in [3] and [10], for example, to be useful diagnostic tools through which to clarify aspects of ocean circulation behaviour.

#### 3.1. Uniform temperature

When  $T$  is uniform, the Stommel–Arons solution results from (2.8), (2.9) and (2.10), and when  $w_s(\lambda, \phi)$  has the uniform value  $w_a$  it is

$$v = w_a \tan \phi/\gamma \quad (3.1.1)$$

$$w = w_a(1 + s) \quad (3.1.2)$$

$$u = 2(\lambda_E - \lambda)w_a \cos \phi/\gamma \quad (3.1.3)$$

It is written here for later comparison with the zero-order ( $\epsilon = 0$ ) solution to be derived as an essential element in the small (but non-zero)  $\epsilon$  solution.

#### 3.2. Zonally uniform temperature

This zero-order ( $\epsilon = 0$ ) solution occurs when the assigned temperature distribution and upwelling velocity at the top of the abyss are independent of  $\lambda$ , i.e.

$$T = T_s(\phi) \text{ and } w = w_s(\phi) \text{ at } s = 0. \quad (3.2.1)$$

This solution is developed in detail in [4] for both the North Atlantic and North Pacific. It is the zero-order element of the solution here and is calculated for the North Atlantic only. When  $T$  is independent of  $\lambda$  then expressions (2.8), (2.9), (2.10)

and equation (2.11) give

$$v = w_s(\phi) \tan \phi / \gamma \quad (3.2.2)$$

$$w = w_s(\phi)(1 + s), \quad (3.2.3)$$

$$-2u \sin \phi = \gamma \left[ \int_{-1}^s \frac{\partial T}{\partial \phi} \partial s' - \int_{-1}^0 \int_{-1}^{s'} \frac{\partial T}{\partial \phi} ds'' ds' \right] + \frac{2(\lambda - \lambda_E)}{\gamma} \frac{d}{d\phi} [w_s(\phi) \sin^2 \phi], \quad (3.2.4)$$

$$w_s(\phi) \left[ (1 + s) \frac{\partial T}{\partial s} + \tan \phi \frac{\partial T}{\partial \phi} \right] = \bar{\beta} \frac{\partial^2 T}{\partial s^2}, \quad (3.2.5)$$

where  $v, w$  are determined independently of the temperature,  $T$ , and equation (3.2.5) for  $T$  is linear. When temperature,  $T$ , has been determined through solving equation (3.2.5) numerically, then  $u$  is given by expression (3.2.4). On the right-hand side of (3.2.4) the integral terms represent thermal wind effects (ignored in [12] and [13]), while the other term represents the effect of upwelling (simplified in [12] and [13] by replacing  $w_s(\phi)$  by a constant  $w_a$ ).

The equations for the streamlines are

$$\cos \phi d\lambda / u = d\phi / v = \gamma ds / w, \quad (3.2.6)$$

where the latter two equations give  $ds/d\phi = w/\gamma v = (1 + s)/\tan \phi$  and which integrates to give

$$s = -1 + c_1 \sin \phi. \quad (3.2.7)$$

Different values of the constant  $c_1$  give the curves in the  $(z, \phi)$  plane along which the  $(v, w)$  field flows (for both the case here and the Stommel–Arons case). This  $(v, w)$  flow field is shown in Fig. 1, where the arrows indicate the direction of flow. The curves  $c_1 = 0$  (ocean bottom) and  $c_1 = 2/\sqrt{3}$  are marked in Fig. 1 in the latitude range  $0 \leq \phi \leq 60^\circ \text{N}$ .

The validity of the planetary geostrophic equations (based on the assumption that the magnitude of the planetary vorticity is much larger than the magnitude of the relative vorticity) does not extend to the equator, since there the Coriolis parameter  $f = 2\Omega \sin \phi$  ( $\Omega$ : earth's rotation rate) vanishes. Despite this, the solutions derived here are not singular at the equator (however, all  $(v, w)$  streamlines in Fig. 1 do emanate from the sea floor at the equator) and, on this basis, the planetary geostrophic equations are, here, extended to the equator. To derive the correct solutions near the equator (say, within  $5^\circ$  of the equator) it is necessary to represent correctly the dynamics in the immediate vicinity of the equator. Also there is no flow across the equator ( $v$  vanishes there), which is consistent with observations that show flow across the equator mainly in the western boundary current, which is not resolved in the model here.

The first two equations in (3.2.6) give  $\cos \phi d\lambda/d\phi = u/v$ . On substitution for  $u$ , given by (3.2.4), and  $v$ , given by (3.2.2), the resulting first-order ordinary differential equation is linear in  $\lambda$  and has an integrating factor which can be evaluated exactly,

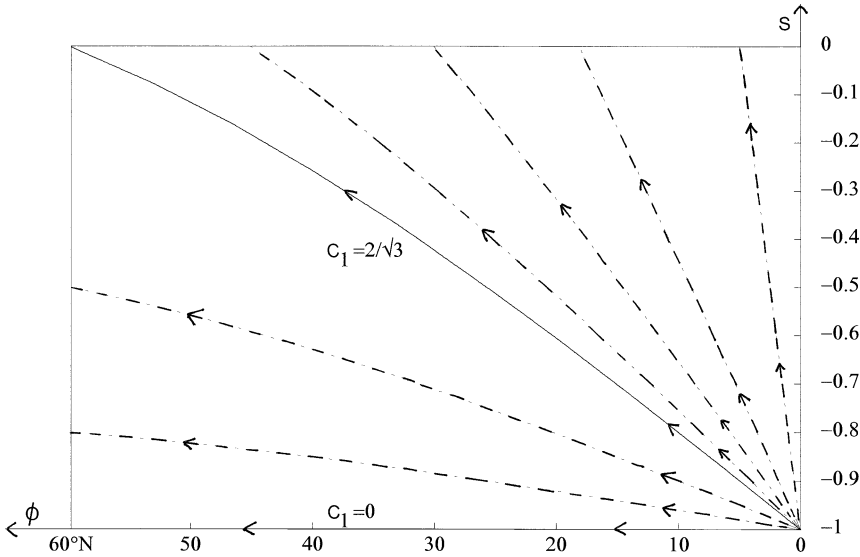


FIG. 1—The directions of the meridional-vertical ( $v, w$ ) flow field as given by the characteristic curves (3.2.7). The arrows indicate the direction of flow, and the curves  $c_1 = 0$  (ocean bottom) and  $c_1 = 2/\sqrt{3}$  are marked for future reference. The variable  $s = z/y$ .

leading to the solution

$$\lambda - \lambda_E = \frac{c_2 + \gamma^2 \int_0^\phi \left[ \int_{-1}^s \int_{-1}^s \frac{\partial T}{\partial \phi'} ds' ds - \int_{-1}^s \frac{\partial T}{\partial \phi'} ds' \right] d\phi'}{2w_s(\phi) \sin 2\phi}. \quad (3.2.8)$$

Expression (3.2.8) gives the equations of the streamlines (for different values of the constant  $c_2$ ) when  $s$  (which appears as the upper limit in the second integral on the right-hand side of (3.2.8)) is on a characteristic curve as given by (3.2.7), i.e.  $s = -1 + c_1 \sin \phi$ . The characteristic curves  $c_1 = 0$  and  $c_1 = 2/\sqrt{3}$  are marked on Fig. 1. When  $T$  has been determined, through the numerical solution of equation (3.2.5), expression (3.2.8) is used, later, to plot the streamlines for the North Atlantic on the characteristic curves  $c_1 = 0$  (ocean bottom) and  $c_1 = 2/\sqrt{3}$  (marked on Fig. 1).

In the case where  $T$  is constant and  $w_s(\phi) = w_a$  (constant) expression (3.2.8) gives the streamlines for the Stommel-Arons solution to be

$$\lambda = \lambda_E = A/\sin^2 \phi, \quad (3.2.9)$$

where  $A$  is an arbitrary constant. Different values of the constant  $A$  give the curves in the  $(\lambda, \phi)$  plane along which the  $(u, v)$  field (for the Stommel-Arons solution) flows and are shown in Fig. 2, where the arrows indicate the direction of flow. Figure 2 also gives the streamlines on the ocean bottom (since there  $w = 0$ ) and, since (3.2.9) is independent of  $z$ , Fig. 2 also gives the streamlines above the ocean bottom except

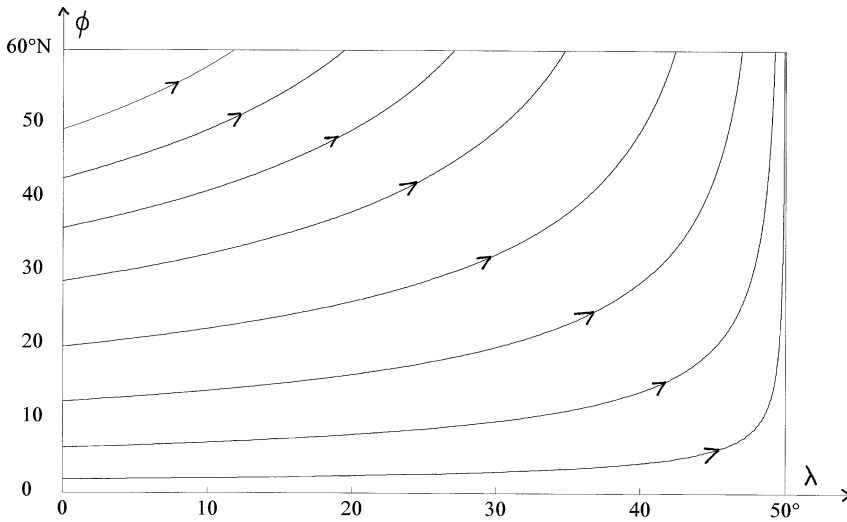


FIG. 2—Streamlines on the ocean bottom for the North Atlantic as given by the Stommel–Arons solution (3.1.1) and (3.1.3).

that these lie on the constant  $c_1$  curves shown in Fig. 1 when  $c_1 \neq 0$  ( $c_1 = 0$  is the ocean bottom). Figure 2 has  $\lambda_E = 5\pi/18$  to represent the North Atlantic.

### 3.3. Zero-order solution for the temperature

From the climatological data in [6, fig. 16, p. 122] showing annual mean potential temperature ( $^{\circ}\text{C}$ ) at 1500m depth we take, for the North Atlantic, the temperature distribution at the top of the abyss (cf. (3.2.1)) to be given by

$$\begin{aligned} T_s(\phi) &= 1 + 1.82\phi^2 && \text{when } 0 \leq \phi \leq \pi/6, \\ &= 1.75 - 0.91\phi^2 && \text{when } \frac{\pi}{6} \leq \phi \leq \pi/3. \end{aligned} \quad (3.3.1)$$

Note that the reference temperature for the North Atlantic is  $t'_0 = 2.0^{\circ}\text{C}$  so that (3.3.1) gives the temperature at the top of the abyss increasing quadratically from  $4^{\circ}\text{C}$  at the equator to  $5^{\circ}\text{C}$  at  $30^{\circ}\text{N}$  and then decreasing quadratically from there to  $3.5^{\circ}\text{C}$  at  $60^{\circ}\text{N}$ . In fact in the later numerical solution of equation (3.2.5) it is necessary to smooth expression (3.3.1) for  $T_s(\phi)$  near  $\phi = \pi/6$  so that  $dT_s(\phi)/d\phi$  is continuous at  $\phi = \pi/6$ , but this detail is not included in expression (3.3.1).

The shape of the upwelling function,  $w_s(\phi)$ , at the top of the abyss (cf. (3.2.1)) is chosen as follows. Since the thermocline is shallower at the equator than at  $60^{\circ}\text{N}$ , and since theoretical predictions give the upwelling velocity varying as  $k'_z/d$  where  $k'_z$  is the coefficient of thermal diffusion and  $d$  is the thickness of the thermocline layer, this implies a larger upwelling velocity at the equator than at  $60^{\circ}\text{N}$ . We therefore take  $w_s(\phi)$  to decrease linearly from the equator to  $60^{\circ}\text{N}$ , i.e. given by

$$w_s(\phi) = m\phi + c, \quad (3.3.2)$$

where  $m(< 0)$ ,  $c$  are parameters chosen later. However, near the equator (for  $\phi \leq 5^\circ$ ) the linear expression (3.3.2) for  $w_s(\phi)$  is replaced by a quadratic representation. The above expression (3.3.2) giving the upwelling decreasing continuously towards the north is consistent with results from [5] which show upwelling decreasing from the equator northwards (and also decreasing westwards from the eastern boundary).

We require that the total upwelling through the surface of the abyss (i.e. the region  $0 \leq \lambda \leq \lambda_E$  and  $0 \leq \phi \leq \pi/3$ ) as given by expression (3.3.2) for  $w_s(\phi)$  (scaled with the upwelling velocity  $W = 2 \times 10^{-7} \text{ m s}^{-1}$ ) should equal the Stommel–Arons uniform upwelling given by  $w_s(\phi) \equiv w_a = 1$  (when scaled with respect to  $W = 2 \times 10^{-7} \text{ m s}^{-1}$ ). This requires

$$\int_{\lambda=0}^{\lambda=\lambda_E} \int_{\phi=0}^{\phi=\pi/3} \cos \phi d\phi d\lambda = \int_{\lambda=0}^{\lambda=\lambda_E} \int_{\phi=0}^{\phi=\pi/3} (m\phi + c) \cos \phi d\phi d\lambda, \quad (3.3.3)$$

which yields

$$m = 2.13(1 - c) \text{ or } c = 1 - 0.47m. \quad (3.3.4)$$

The term on the left in equation (3.3.3) represents the upwelling through the surface of the abyss over the total ocean region in the Stommel–Arons uniform upwelling case, while the right-hand side of (3.3.3) represents the same quantity in the model here.

The parabolic partial differential equation (3.2.5) for  $T$  is now solved numerically (using the NAG FORTRAN Library Routine DO3PAF) with the boundary condition  $T = T_s(\phi)$  at  $s = 0$  and  $T = 0$  at  $s = -1$  together with the symmetry condition  $\partial T / \partial \phi = 0$  at  $\phi = 0$  (the equator). Note that near the equator (for  $\phi \leq 5^\circ$ ) the linear representation (3.3.2) for  $w_s(\phi)$  is replaced by a quadratic representation. This is necessary to ensure that the condition  $\partial T / \partial \phi = 0$  at  $\phi = 0$  is satisfied. Since  $c = 1 - 0.47$  (cf. (3.3.4)) expression (3.3.2) for  $w_s(\phi)$  contains only one variable parameter, i.e.  $m(< 0)$ . Therefore equation (3.2.5) for  $T$  contains two parameters,  $m$ ,  $\bar{\beta}$ . A series of numerical experiments, by varying the values of  $m$ ,  $\bar{\beta}$ , is performed in solving equation (3.2.5) until a temperature distribution is identified which is acceptably close to the climatological data given in [6]. These data are shown in [6, fig. 110, p. 158], where the annual mean zonally averaged temperature distribution for the North Atlantic is displayed. These numerical experiments yield  $\bar{\beta} = 0.25$  (gives thermal diffusion coefficient,  $k'_z = 1.25 \times 10^{-4} \text{ m}^2 \text{ s}^{-1}$ ) and  $m = -0.7$  (gives upwelling velocity at the equator of  $2.6578 \times 10^{-7} \text{ m s}^{-1}$ .) The corresponding temperature field is shown in Fig. 3 and is seen to be in reasonable agreement with [6, fig. 110, p. 158].

The values of  $\bar{\beta}$  and  $m$  (and hence  $k'_z$  and  $w_s(\phi)$ ) are not determined uniquely by the above procedure. The numerical experimentation began from the base of very small  $\bar{\beta}$  and  $m$ , i.e. near the Stommel–Arons uniform upwelling solution which has  $\bar{\beta} = m = 0$ . The identification of the temperature distribution shown in Fig. 3 (with  $\partial T / \partial \phi > 0$  in the southern ocean and  $\partial T / \partial \phi < 0$  in the northern ocean) arose as follows. When  $\bar{\beta}$  is too small (ex.  $\bar{\beta} = 0.1$ ) the isotherms are more crowded near the upper boundary than occurs in [6, fig. 110] and when  $\bar{\beta}$  is too large (ex.  $\bar{\beta} = 0.4$ ) the isotherms show almost linear separation with depth, unlike what is shown in

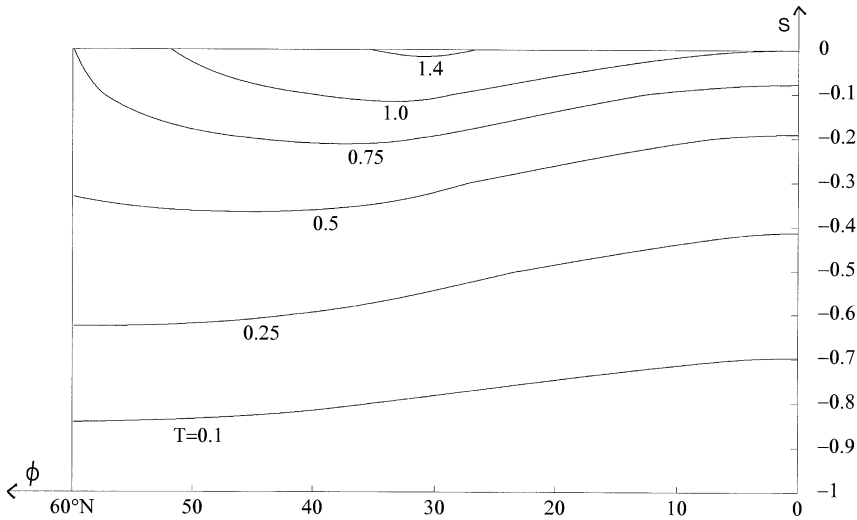


FIG. 3—Temperature distribution for the abyssal region of the North Atlantic.

[6, fig. 110]. For reasonable representation of  $T$  the parameter  $\bar{\beta}$  may have values in the range  $0.2 \leq \bar{\beta} \leq 0.3$ . The distribution of  $T$  is less sensitive to variation in the value of  $m$ . However, a value of  $m$  sizeable in magnitude is necessary in order to create the substantial variation of temperature with latitude (near the equator) shown in Fig. 3 (which accords with [6, fig. 110]). Although Fig. 3 is created with  $m = -0.7$ , a not too dissimilar picture occurs when  $m = -0.3$ .

#### 3.4. Zero-order zonal velocity

With temperature,  $T$ , now determined, the zonal component of velocity,  $u$ , is given numerically through expression (3.2.4). It is interesting in expression (3.2.4) for  $u$  to consider the relative importance of the thermal wind term (multiplied by a factor  $\gamma = 6.643$ ) and the upwelling term (divided by a factor  $\gamma$ ). It transpires that the thermal wind term is important everywhere. This is confirmed in the later figures displaying distributions of  $u$ . In contrast, the upwelling term is the only term in the Stommel–Arons solution. Another contrast is with a thermocline model (which these equations can also represent) as in [16], where for a thermocline of depth 800m the wind-stress term (equivalent to upwelling term) is dominant except near the eastern boundary, where thermal wind becomes important. The distributions for  $u$  are shown in Fig. 4 (at  $\lambda = 0$ , western boundary) and Fig. 5 (at  $\lambda = \lambda_E$ , eastern boundary with  $\lambda_E = 5\pi/18$ ). Areas of negative  $u$  (westward flow) are shaded. For future reference (related to drawing streamlines) the characteristic curve  $c_1 = 2/\sqrt{3}$  from Fig. 1 is marked on Figs 4 and 5. These distributions of  $u$  can be compared with the Stommel–Arons expression for  $u$  as given by (3.1.3) with  $w_a = 1$ . This gives  $u$  positive (eastward) everywhere, zero at the eastern boundary, independent of depth and decreasing in value towards the north. It has a maximum value of  $u_m$  when  $\lambda = 0$  and  $\phi = 0$  where  $u_m = 2\lambda_E/\gamma = 0.2627$ , which in physical variables

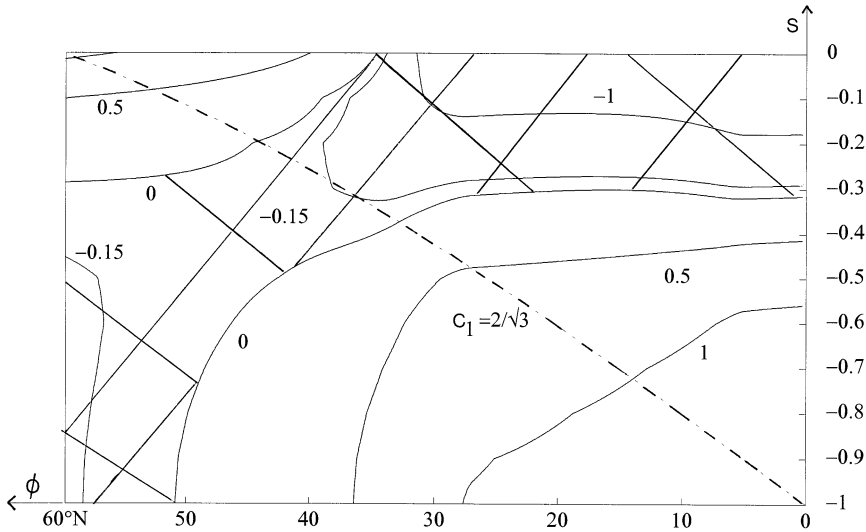


FIG. 4—Distribution of the zonal velocity,  $u$ , at the western boundary ( $\lambda = 0$ ) for the North Atlantic. The characteristic curve  $c_1 = 2/\sqrt{3}$ , as given in Fig. 1, is marked here and on Fig. 5. Areas where  $u$  is negative (westward flow) are shaded.

is  $0.880 \times 10^{-3} \text{ m s}^{-1}$ . In Figs 4 and 5  $u$  is non-uniform with depth. These figures show eastward flow in the lower portion of the southern ocean which is returned at the eastern boundary as westward flow in the upper portion of the southern ocean. In the northern ocean there is flow towards the east in the upper ocean which is returned at the eastern boundary as westward flow in the lower portion of the water column. A feature of Figs 4 and 5 is that the picture at  $\lambda = \lambda_E$  (Fig. 5), where the upwelling term in  $u$  vanishes, is not significantly different from the picture at  $\lambda = 0$  (Fig. 4), where the upwelling term has its maximum value. This implies that, in the North Atlantic, the upwelling term in  $u$ , while not negligible, is also not very significant.

### 3.5. Zero-order streamlines

The streamlines for Stommel and Arons ([12]; 13]) were calculated in section 3.2 and are shown in Fig. 2 on the ocean bottom. The streamlines above the ocean bottom are also given by Fig. 2 except that they lie on the characteristic curves  $s = -1 + c_1 \sin \phi$  (shown in Fig. 1) when  $c_1 \neq 0$  ( $c_1 = 0$  is the ocean bottom). Also described in section 3.2 is the procedure used to plot the streamlines here (using expression (3.2.8)) and they are shown in Figs 6 and 7 on the characteristic curves  $c_1 = 0$  (ocean bottom) and  $c_1 = 2/\sqrt{3}$  (marked on Fig. 1) respectively.

Figure 6 shows eastward flow (flow is always eastward in the Stommel–Arons solution; cf. Fig. 2) entering the eastern boundary between the equator and the point  $A$ , with westward flow issuing from the eastern boundary between  $A$  and  $\phi = 60^\circ \text{ N}$ . The curve  $u = 0$  is marked on Fig. 6, south of which  $u > 0$  (i.e. eastward flow) and north of which  $u < 0$  (i.e. westward flow). The picture in Fig. 6 is fundamentally

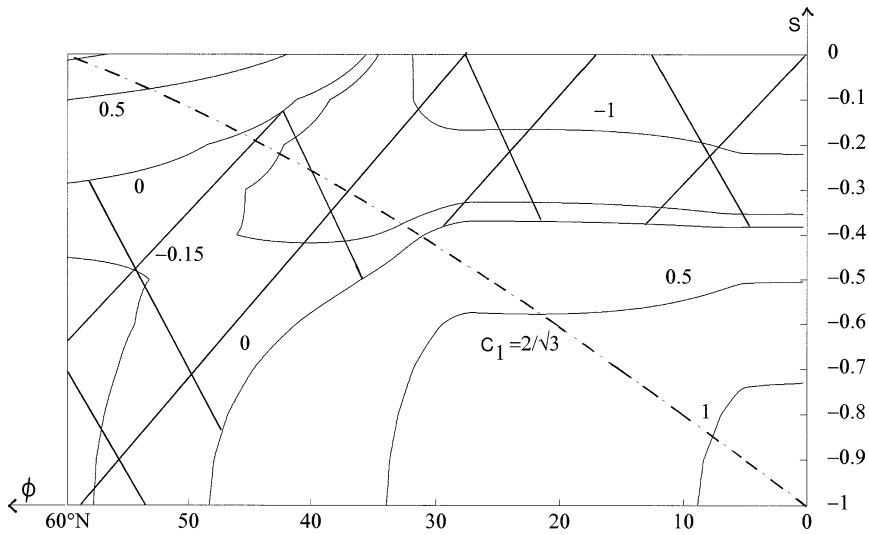


FIG. 5—Distribution of  $u$  at  $\lambda = \lambda_E = 50^\circ$  (the eastern boundary) for the North Atlantic. The shaded areas mark where  $u$  is negative.

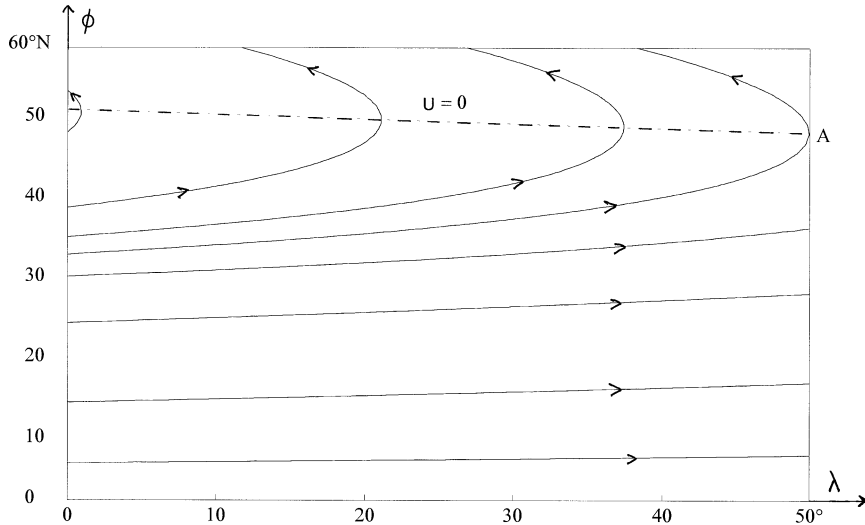


FIG. 6—Streamlines on the ocean bottom for the North Atlantic.

different to that in Fig. 2 (Stommel–Arns solution) owing to the fact that thermal wind effects (neglected in Stommel–Arns) are of major importance here.

Figure 7 shows the streamlines on the characteristic curve  $c_1 = 2/\sqrt{3}$  (marked on Fig. 1), i.e. when  $s = -1 + 2 \sin \phi / \sqrt{3}$ . There are two curves  $u = 0$  marked on Fig. 7 and between them the flow is westward; to the south of them the flow is

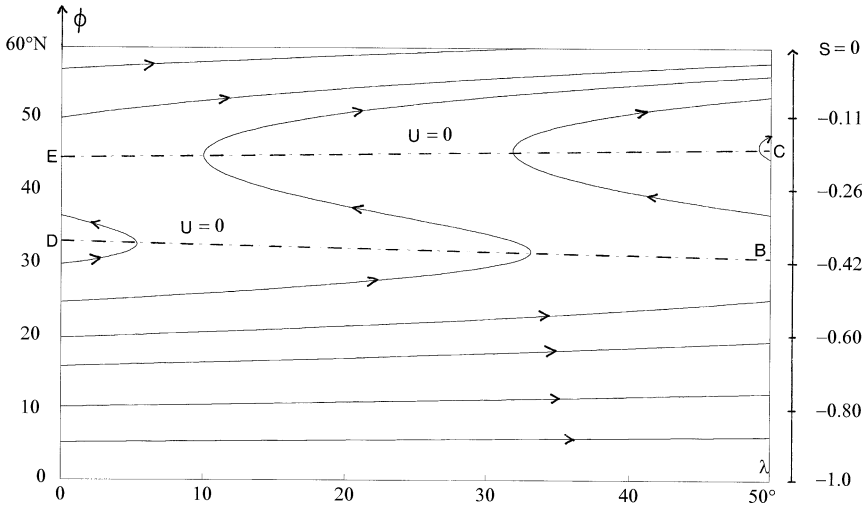


FIG. 7—Streamlines for the North Atlantic on the characteristic curve  $c_1 = 2/\sqrt{3}$  (cf. Fig. 1), i.e. when  $s = -1 + 2 \sin \phi/\sqrt{3}$  where  $s = z/y$ . For convenience the non-linear relationship between  $s$  and  $\phi$  is marked on the right side of the figure.

eastward, and north of them the flow is eastward. At the western boundary there is outflow between the equator and point  $D$ , inflow between points  $D$  and  $E$ , and outflow between  $E$  and  $\phi = 60^\circ$  N. At the eastern boundary there is inflow between the equator and point  $B$ , outflow between points  $B$  and  $C$ , and inflow between point  $C$  and  $\phi = 60^\circ$  N. This streamline picture is totally different to the Stommel–Arons solution shown in Fig. 2.

### 3.6. Comparison with some other results and observations

The results from this zero-order model of the abyssal circulation can be compared with some observational results for the North Atlantic contained in [14] and with some results from the three-dimensional numerical model of the North Atlantic circulation given in [1].

A notable feature of the flow at the bottom of the abyss (here at depth 4000m) shown in Fig. 6 for the North Atlantic is the eastward flow from the western boundary (between the equator and  $30^\circ$  N) into the eastern boundary (between the equator and approximately  $40^\circ$  N). This is consistent with the eastward spreading of Antarctic Bottom water shown in [14, pls 19–25].

Figure 7 shows the flow in the North Atlantic at intermediate depths (i.e. on the curve  $s = -1 + 2 \sin \phi/\sqrt{3}$  where  $s = -1$  is the bottom of the abyss at 4000m depth). A prominent feature is the westward flow from the eastern boundary between points  $B$  (approx.  $30^\circ$  N) and  $C$  (approx.  $45^\circ$  N) into the western boundary between points  $D$  and  $E$ . The depth at point  $B$  is 2557m and at point  $C$  is 1959m. This flow is consistent with the westward progression of the Mediterranean outflow at about that depth shown in [14, pls 33, 35, 37, 39, 41]. There is, of course, no Mediterranean

outflow included in the model here, but in the sense that Mediterranean salt water can be viewed as a passive tracer of the velocity field it is reasonable to compare the velocity field here with that shown in [14]. A similar westward jet across the entire North Atlantic in the latitude range  $25^\circ\text{N}$  to  $32^\circ\text{N}$  over the depth 1000m to 2000m is reported in [1]. It is noted in [1] that this feature supports the qualitative conjecture by Wust ([15]) of flow along the ‘Mediterranean Salt Tongue’ which extends westward across the North Atlantic from the Straits of Gibraltar, as seen graphically in [14, pl. 43]. Strong flow of magnitude  $10^{-2}\text{ m s}^{-1}$  in this westward jet is reported in [1]. These values are consistent with the flow issuing from the eastern boundary of the North Atlantic (Fig. 5), where at the top of the abyss ( $s = 0$ , i.e. depth 1500m) at  $30^\circ\text{N}$   $u = -1.66$  (corresponds to a dimensional value of  $0.5561 \times 10^{-2}\text{ m s}^{-1}$ ).

Another feature of the flow in Fig. 7 is the eastward flow from the western boundary between the point  $E$  and  $60^\circ\text{N}$  which enters the eastern boundary north of  $50^\circ\text{N}$ . This flow is near the top of the abyss (here at depth 1500m) and enters the eastern boundary (cf. Fig. 5) where  $u$  is approximately 1.0 (corresponds to  $0.335 \times 10^{-2}\text{ m s}^{-1}$ ) in the latitude range  $55^\circ\text{N}$  to  $60^\circ\text{N}$ . Similar eastward flow with similar speeds (at approximately  $50^\circ\text{N}$ ) at a depth of 1000m is reported in [1].

#### 4 Weak zonal variation in temperature

Zonal variation in temperature can be created through zonal variation in assigned temperature distribution and/or upwelling velocity at the top of the abyss. Here, in order to distinguish their particular influences we will treat separately the cases where (a) temperature distribution varies with  $\lambda$  but upwelling velocity is independent of  $\lambda$ , i.e.

$$T = T_s(\lambda, \phi) \text{ and } w = w_s(\phi) \text{ at } s = 0, \quad (4.1)$$

and (b) temperature distribution is independent of  $\lambda$  and upwelling velocity varies with  $\lambda$ , i.e.

$$T = T_s(\phi) \text{ and } w = w_s(\lambda, \phi) \text{ at } s = 0. \quad (4.2)$$

The combined case of temperature distribution and upwelling velocity both varying with  $\lambda$  (and not considered here) is then clearly treated in a similar fashion.

##### 4.1. Zonal variation only in $T_s$

Here, we perturb the zero-order problem considered in section 3 by writing the assigned temperature distribution and upwelling velocity at the top of the abyss in the form

$$T = T_s(\phi) + \epsilon(\lambda/\lambda_E)\sin^3 3\phi \text{ at } s = 0, \quad (4.1.1)$$

where  $T_s(\phi)$  is the zero-order distribution given by (3.3.1) and  $\epsilon$  is a small positive parameter, to be determined, while

$$w = w_s(\phi) = 1.32 - 0.7\phi \text{ at } s = 0, \quad (4.1.2)$$

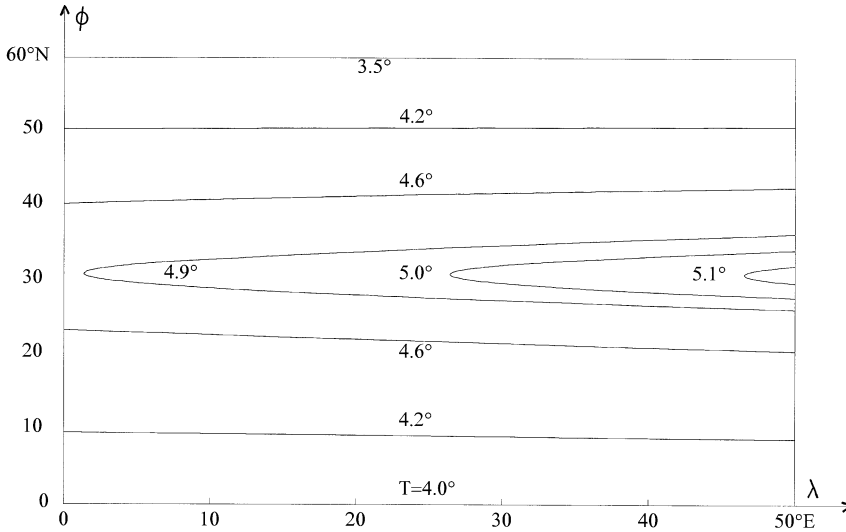


FIG. 8—Assigned temperature distribution at the top of the abyss as given by expression (4.1.1) for  $\epsilon = 0.1$  and showing at the western boundary ( $\lambda = 0$ ) the zero-order temperature distribution increasing from  $4^\circ\text{C}$  at the equator to  $5^\circ\text{C}$  at  $30^\circ\text{N}$  and then decreasing from there to  $3.5^\circ\text{C}$  at  $60^\circ\text{N}$ . This is combined with weak zonal variation which is seen to be a reasonably qualitative (but not detailed) representation of the climatological data [6, fig. 16, p. 122] showing annual mean potential temperature ( $^\circ\text{C}$ ) at 1500m depth.

where  $w_s(\phi)$  is the zero-order upwelling velocity used in section 3.3. The temperature distribution at the top of the abyss as given by (4.1.1) for  $\epsilon = 0.1$  (largest value of  $\epsilon$  for which the numerical iteration procedure converges to a solution) is shown in Fig. 8 and is seen to represent qualitatively (but not in detail) the climatological data in [6, fig. 16, p. 122] showing annual mean potential temperature ( $^\circ\text{C}$ ) at 1500m depth. The full non-linear equation (2.11) with  $v, w, u$  as given by expressions (2.8), (2.9), (2.10) is now solved by the iteration procedure described in Appendix A for a series of increasing values of  $\epsilon$  from  $\epsilon = 0$ . It transpires that the largest value of  $\epsilon$  for which this numerical iteration procedure converges to a solution is  $\epsilon = 0.1$ . For values of  $\epsilon > 0.1$  either the numerical algorithm fails to produce a solution or the solutions produced vary too much from one iteration of the process to the next so that the condition specified in Appendix A is not satisfied.

Figure 9 shows the temperature distribution at the western boundary ( $\lambda = 0$ ) and eastern boundary ( $\lambda = \lambda_E$ ) where there is detectable *downward bowing* of isotherms towards the east in the northern ocean (giving  $\partial T / \partial \lambda > 0$  similar to what occurs at the surface  $s = 0$  in expression (4.1.1)) with no detectable zonal variation in isotherms occurring in the southern ocean (within approximately 15 degrees of the equator). On overlaying Fig. 9 on Fig. 3 it is seen that there is a larger change between Fig. 9 (temperatures at western and eastern boundaries) and the zero-order temperature shown in Fig. 3 than between the temperature distributions shown in Fig. 9. These facts are consistent with the major change produced in the meridional

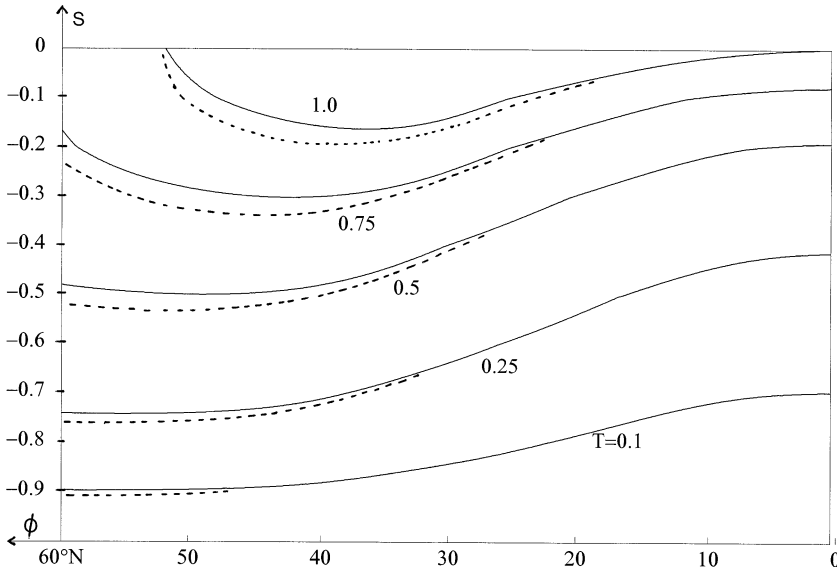


FIG. 9—Temperature distribution (solid curves) at the western boundary ( $\lambda = 0$ ) and at the eastern boundary ( $\lambda = \lambda_E$ ; dotted curves) for the case  $\epsilon = 0.1$ .

velocity,  $v$  (from the zero-order case given by (3.2.2) which is independent of depth), as a result of the small zonal variation in  $T$ . These changes are shown in Fig. 10 (shows  $v$  at the western boundary,  $\lambda = 0$  and eastern boundary  $\lambda = \lambda_E$  with depth-invariant zero-order  $v$  given by (3.2.2) plotted for comparison). As a result of these changes in  $v$  the advection term  $\gamma v \partial T / \partial \phi$  appearing in the heat equation (2.11) is significantly altered from its zero-order state. We note that the changes in  $v$  (from its zero-order state) occurring in Fig. 10 (at  $\lambda = 0$  and  $\lambda = \lambda_E$ ) are in the approximate latitude range ( $15^\circ \text{ N} < \phi \leq 60^\circ \text{ N}$ ) which is consistent with Fig. 9 ( $T$  at  $\lambda = 0$  and  $\lambda = \lambda_E$ ), showing  $T$  almost zonally invariant *outside* this latitude range (i.e. *inside*  $0 \leq \phi \leq 15^\circ \text{ N}$ ).

The distributions of  $v$  at  $\lambda = 0$  and at  $\lambda = \lambda_E$  in Fig. 10 are comparable with some results shown in [9]. Our results (with thermal diffusion coefficient,  $k'_z = 1.25 \times 10^{-4} \text{ m}^2 \text{ s}^{-1}$ ), which lie between the results given in [9, fig. 2(b)] (with  $k'_z = 40 \times 10^{-4} \text{ m}^2 \text{ s}^{-1}$  and uniform upwelling) and [9, fig. 2(c)] (with  $k'_z = 0.4 \times 10^{-4} \text{ m}^2 \text{ s}^{-1}$  and uniform upwelling), are nearer the [9, fig. 2(c)] results (given at latitude  $\phi = 30^\circ \text{ N}$  and longitude  $\lambda = \lambda_E/4$ ). Both [9, fig. 2(c)] and our Fig. 10 show (at  $\phi = 30^\circ \text{ N}$ ) most of the variation of  $v$  occurring in the upper ocean. Our results show  $v$  decreasing by a factor of 5 between  $s = 0$  (surface) and  $s = -0.6$ , with  $v$  exhibiting similar variation in [9, fig. 2(c)]. In [9, fig. 2(c)] there is a region of negative  $v$  (between  $s = -0.4$  and  $s = -0.8$ ) which does not occur in Fig. 10, but our results lie between [9, fig. 2(c)] and [9, fig. 2(b)], where the latter shows  $v$  positive over the whole water column as occurs in our Fig. 10.

Figure 11 shows the vertical velocity,  $w$ , distribution at the western ( $\lambda = 0$ )

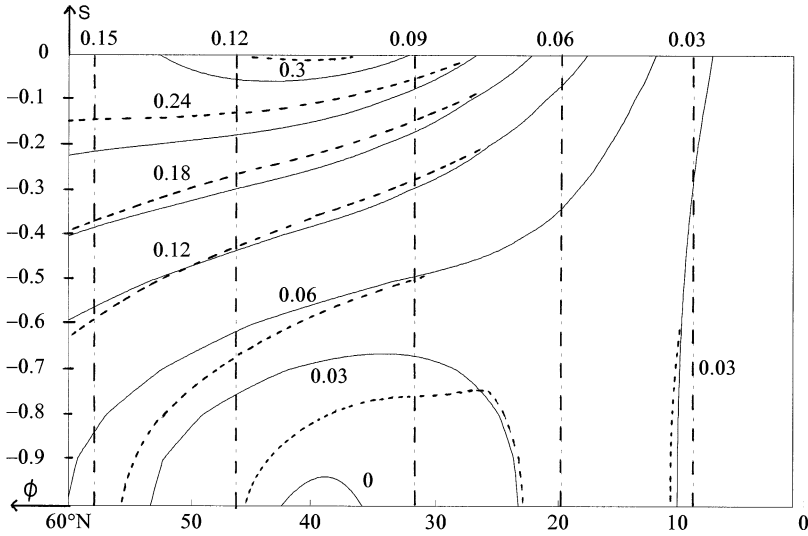


FIG. 10—(a) Distribution of meridional velocity,  $v$  (solid curves), at the western boundary ( $\lambda = 0$ ). Note the small region of negative  $v$  near  $s = -1$  in the northern ocean. (b) Distribution of meridional velocity,  $v$  (dotted curves), at the eastern boundary ( $\lambda = \lambda_E$ ). Note that curve  $v = 0.3$  is, here, nearer the surface ( $s = 0$ ) than at the western boundary  $\lambda = 0$ . Also, the small region of negative  $v$  near  $s = -1$  occurring at the western boundary,  $\lambda = 0$ , has disappeared here. The zero-order depth-invariant  $v$  given by (3.2.2) is shown for comparison (dashed lines).

and the eastern boundary ( $\lambda = \lambda_E$ ), with detectable difference (i.e. variation with  $\lambda$ ) between these distributions. For comparison, the zero-order  $w$  given by (3.2.3) (varies linearly with depth) is also plotted in Fig. 11, showing larger variation between it and  $w$  at  $\lambda = 0$  (Fig. 11) than between  $w$  at  $\lambda = 0$  and at  $\lambda = \lambda_E$  (in Fig. 11). We note that these differences are largest away from the equator region. As a result of these changes in  $w$  the advection term  $w\partial T/\partial s$  appearing in the heat equation (2.11) is significantly altered from its zero-order state and contributes to the significant difference between the zero-order temperature shown in Fig. 3 and the temperature distributions at  $\lambda = 0$ , and  $\lambda = \lambda_E$ , shown in Fig. 9.

Again these distributions of  $w$  at  $\lambda = 0$  and at  $\lambda = \lambda_E$  (Fig. 11) are comparable with and consistent with [9, fig. 2(c)], where all figures show most of the variation of  $w$  occurring in the upper ocean above  $s = -0.5$  (except near the equator).

Figure 12 shows the zonal velocity,  $u$ , at the western boundary ( $\lambda = 0$ ) and is most significantly different to the zero-order  $u$  at  $\lambda = 0$  shown in Fig. 4. Figure 13 shows the zonal velocity,  $u$ , at the eastern boundary ( $\lambda = \lambda_E$ ) and shows substantial change (especially increased magnitudes for  $u$ ) from the zero-order  $u$  at  $\lambda = \lambda_E$  shown in Fig. 5.

#### 4.2. Zonal variation only in $w_s$

Here we perturb the zero-order problem considered in section 3 by allowing the assigned upwelling velocity at the top of the abyss to vary with  $\lambda$  but maintain

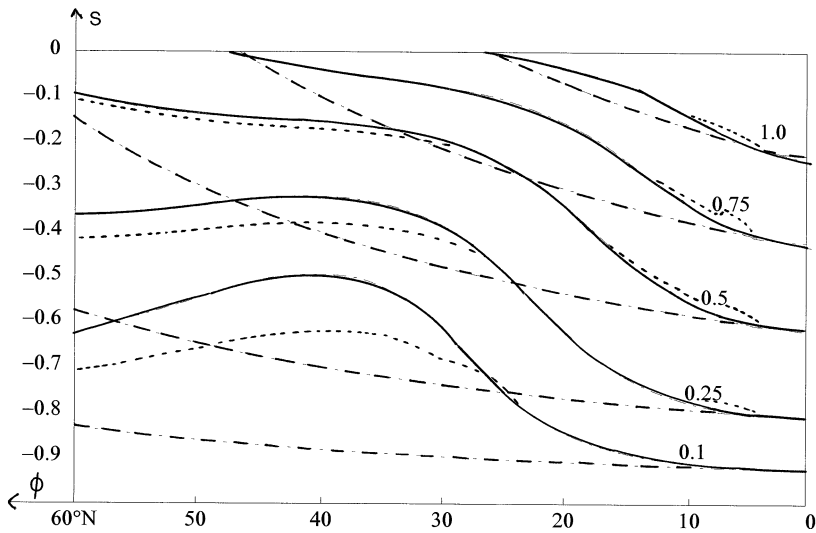


FIG. 11—(a) Distribution of vertical velocity,  $w$  (solid curves), at the western boundary,  $\lambda = 0$ , and (b) distribution of vertical velocity,  $w$  (dotted curves), at the eastern boundary ( $\lambda = \lambda_E$ ), showing detectable variation in the northern ocean. For comparison, the zero-order  $w$  given by (3.2.3) and which varies linearly with depth is also shown (dashed curves).

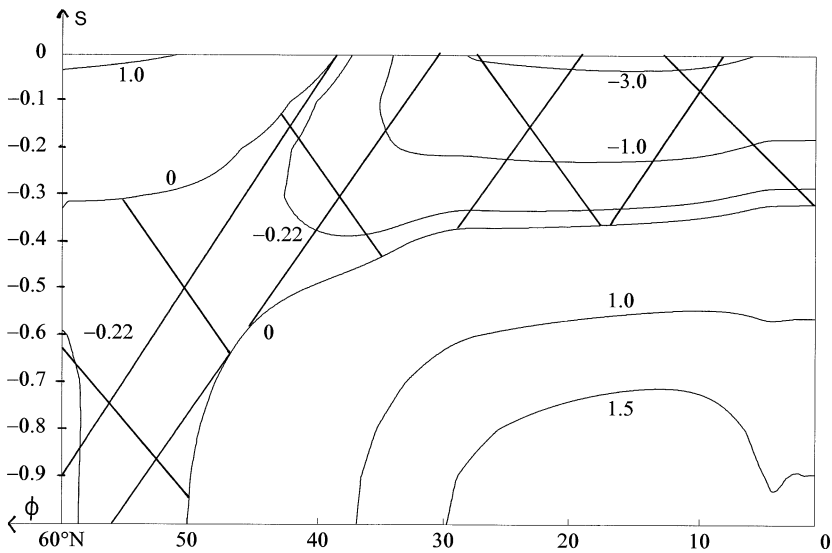


FIG. 12—Distribution of zonal velocity,  $u$ , at the western boundary ( $\lambda = 0$ ). Areas where  $u$  is negative (westward flow) are shaded.

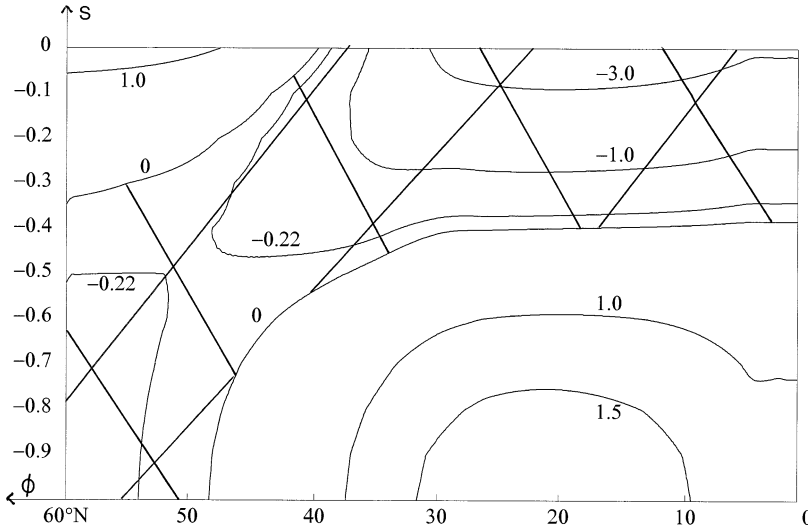


FIG. 13—Distribution of zonal velocity,  $u$ , at the eastern boundary ( $\lambda = \lambda_E$ ). Area where  $u$  is negative is shaded.

the temperature distribution at the top of the abyss at its zero-order distribution  $T_s(\phi)$  given by (3.3.1). The upwelling velocity  $w_s(\lambda, \phi)$  is chosen as follows. Pedlosky ([9]) took  $w_s$  to be a function of  $\lambda$  only and to decrease exponentially towards the west from its maximum value at the eastern boundary. Results from [5] show the upwelling velocity decreasing from the equator northwards and decreasing westwards from the eastern boundary. We chose  $w_s(\lambda, \phi)$  to decrease linearly from the equator northward (the zero-order upwelling velocity,  $w_s(\phi)$ , also does so as given by (4.1.2)) and to decrease linearly from the eastern boundary towards the west and to be given by

$$w_s(\lambda, \phi) = (1 - \lambda/\lambda_E)(1.32 + m_w\phi) + (\lambda/\lambda_E)(1.32 + m_e\phi), \quad (4.2.1)$$

where  $m_w$  is the northward slope at the western boundary ( $\lambda = 0$ ) and  $m_e$  is the northward slope at the eastern boundary ( $\lambda = \lambda_E$ ) and  $|m_w| > |m_e|$ . We required that the total upwelling through the surface of the abyss for the above velocity,  $w_s(\lambda, \phi)$ , should equal the total upwelling through the surface of the abyss in the zero-order case (i.e. when  $w_s = w_s(\phi)$ ). This condition fixes one of the constants  $m_e, m_w$ . A non-dimensional measure of zonal variation in  $w_s(\lambda, \phi)$  is the parameter

$$\mu = \frac{w_s(\lambda_E, \pi/3) - w_s(0, \pi/3)}{w_s(\lambda_E, \pi/3)} \equiv \frac{m_e - m_w}{1.26 + m_e}. \quad (4.2.2)$$

Solutions were calculated for a series of increasing values of  $\mu$ , i.e.  $\mu = 0.14, \mu = 0.21$ , until the maximum value of  $\mu$  for which the numerical iteration process converges was identified. This value is  $\mu = 0.33$  (the process does not converge to a solution at  $\mu = 0.35$ ). For values of  $\mu > 0.33$  the solution process fails for the same reasons as detailed in section 4.1 (where the appropriate parameter is  $\epsilon$ ).

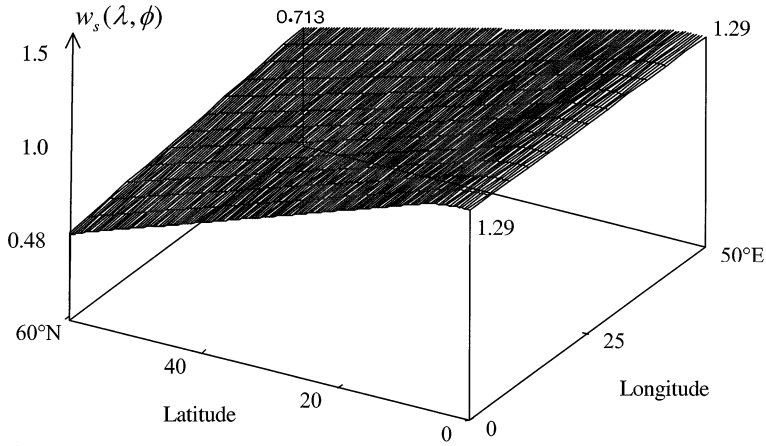


FIG. 14—Assigned upwelling velocity,  $w_s(\lambda, \phi)$ , at the top of the abyss as given by expression (4.2.3) for the case  $\mu = 0.33$ . It shows linear variation with  $\lambda$  and  $\phi$  and includes quadratic smoothing in  $\phi$  near the equator (for  $\phi \leq 5^\circ$ ).

When  $\mu = 0.33$  the expression for  $w_s(\lambda, \phi)$  is

$$w_s(\lambda, \phi) = 1.32 - 0.802\phi + 0.222(\lambda/\lambda_E)\phi. \quad (4.2.3)$$

Near the equator (for  $\phi \leq 5^\circ$ ) the linear representation (4.2.3) for  $w_s(\lambda, \phi)$  is replaced by a quadratic representation in  $\phi$  (recall that similar quadratic smoothing of the zero-order  $w_s(\phi)$  was implemented earlier). The distribution of  $w_s(\lambda, \phi)$  as given by (4.2.3) is shown in Fig. 14 (with quadratic smoothing near the equator included). As was done in section 4.1, the full non-linear equation (2.11) with  $v$ ,  $w$ ,  $u$  as given by expressions (2.8), (2.9), (2.10) is now solved by the iteration procedure described in Appendix A. The only change is that  $w_s(\lambda, \phi)$  given by (4.2.1) now plays the part previously taken by  $T_s(\lambda, \phi)$  given by (4.1.1). The solution is derived for a series of increasing values of  $\mu$  from  $\mu = 0$ . The largest value of  $\mu$  for which convergence of the process occurs is  $\mu = 0.33$  and the results presented below are for  $\mu = 0.33$ .

Figure 15 shows the temperature distribution at the western boundary ( $\lambda = 0$ ) and eastern boundary ( $\lambda = \lambda_E$ ) where there is detectable *upward bowing* of isotherms towards the east (giving  $\partial T/\partial \lambda < 0$ , which is the opposite to what occurs in section (4.1)) except near the surface and equator, where  $\partial T/\partial \lambda = 0$ .

Figure 16 shows  $v$  at the western boundary ( $\lambda = 0$ ) and at the eastern boundary ( $\lambda = \lambda_E$ ) with the zero-order, depth-invariant,  $v$  given by (3.2.2) also plotted there (dashed lines) for comparison. Although the distribution of  $v$  at  $\lambda = 0$  has significantly changed from the depth-invariant zero-order solution, it is noted that the magnitudes of  $v$  have not significantly altered from the zero-order values. At the eastern boundary ( $\lambda = \lambda_E$ ) the striking facts are (i) the significant change from the depth-invariant zero-order solution, (ii) the presence of the negative  $v$  region near the surface in the northern ocean, and (iii) the magnitudes of  $v$  in the lower

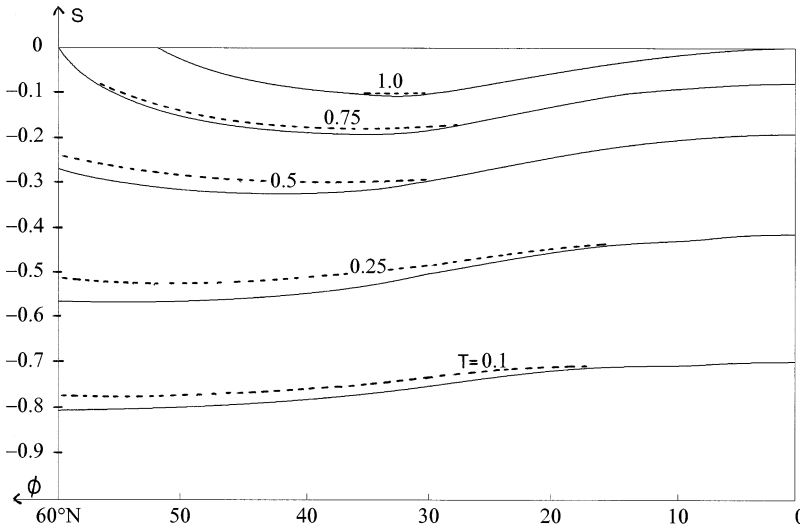


FIG. 15—(a) Temperature distribution (solid curves) at the western boundary ( $\lambda = 0$ ) and (b) temperature distribution (dotted curves) at the eastern boundary ( $\lambda = \lambda_E$ ) for the case  $\mu = 0.33$ .

northern ocean are twice the values of the zero-order  $v$  and the values of  $v$  occurring at the western boundary. The appearance of the southward-flowing water near the surface at the eastern boundary is artificial in the sense that it results from *zonal variation* in the upwelling velocity when the temperature distribution at the top of the abyss is *zonally invariant*. Here we adopted a strategy of separating the influence of zonal variation in upwelling velocity from zonal variation in temperature distribution at the top of the abyss. In reality they both occur together and it is seen here that their separate influences are opposites on both  $T$  and  $v$ . This is so because in section 4.1, where  $T_s$  has zonal variation and  $w_s$  is zonally invariant, then  $\partial T/\partial \lambda > 0$ , leading to  $v$  having a negative region near  $s = -1$  at  $\lambda = 0$  but with  $v$  positive everywhere at  $\lambda = \lambda_E$ , while here, where  $T_s$  is zonally invariant and  $w_s$  has zonal variation, then  $\partial T/\partial \lambda < 0$ , leading to  $v$  having a negative region near  $s = 0$  at  $\lambda = \lambda_E$  but  $v$  is positive everywhere at  $\lambda = 0$ . Attempting to relate the results above to results derived by Pedlosky ([9]) is not sensible since his model assigns  $w_s$  to be zero in the western ocean (after decreasing from its maximum at the eastern boundary), which requires  $v$  to change sign through the water column (in the western ocean). Our solution process, which is a perturbation from a zonally invariant  $w_s$ , is not able to deal with such *large* zonal changes in  $w_s$ . However, the striking result here is that the *small zonal variation* in  $T_s$  allowed in section 4.1 and the *small zonal variation* in  $w_s$  allowed here (section 4.2) both result in *small zonal variation* in  $T$  but which, in turn, produces *very large* changes in  $v$  from its depth-independent, zero-order state. Therefore models involving the planetary geostrophic equations must reflect this fact that when there is even very small zonal variation in  $T$  then  $v$  must be allowed to vary with depth.

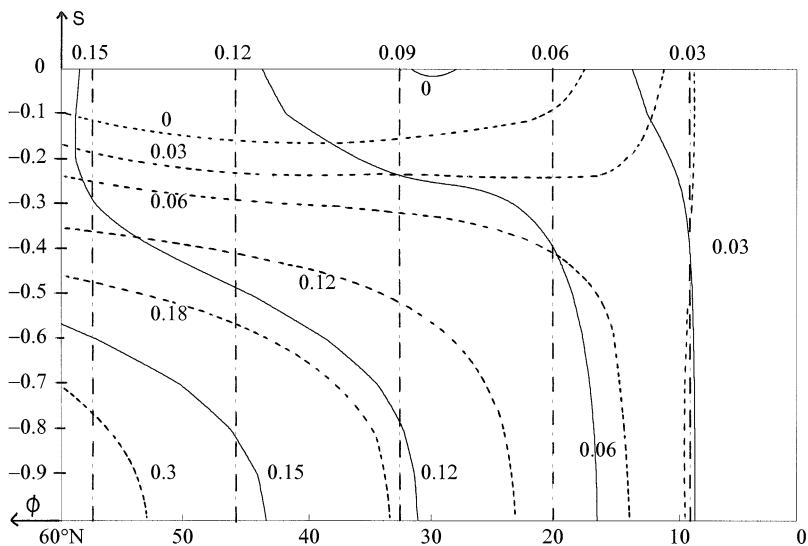


FIG. 16—Distribution of meridional velocity,  $v$  (solid curves), at the western boundary ( $\lambda = 0$ ) and (b) distribution of  $v$  (dotted curves) at the eastern boundary ( $\lambda = \lambda_E$ ) which shows a region of negative  $v$  near the surface in the northern ocean. For comparison, the zero-order depth-invariant  $v$  given by (3.2.2) is also shown (dashed lines).

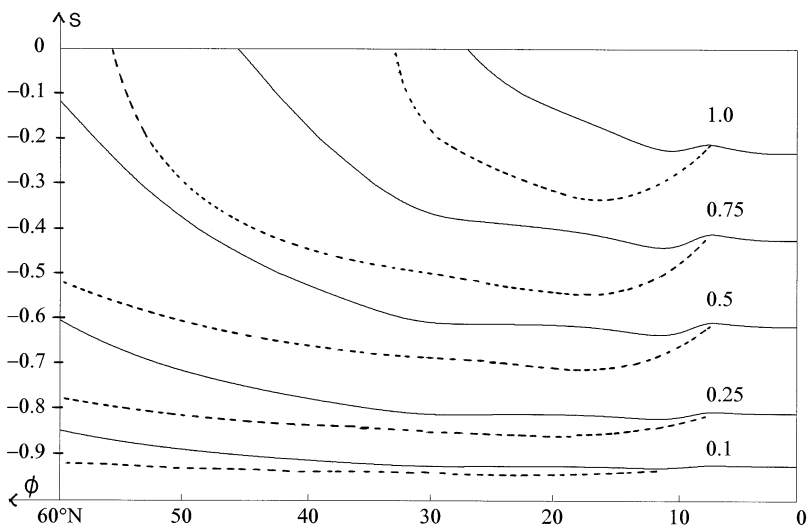


FIG. 17—(a) Distribution of vertical velocity,  $w$  (solid curves), at the western boundary ( $\lambda = 0$ ) and (b) distribution of  $w$  (dotted curves) at the eastern boundary ( $\lambda = \lambda_E$ ), showing significant change from the western boundary distribution outside the equator region. Both these distributions show substantial variation from the zero-order  $w$  given by (3.2.3) and shown (dashed curves) in Fig. 11.

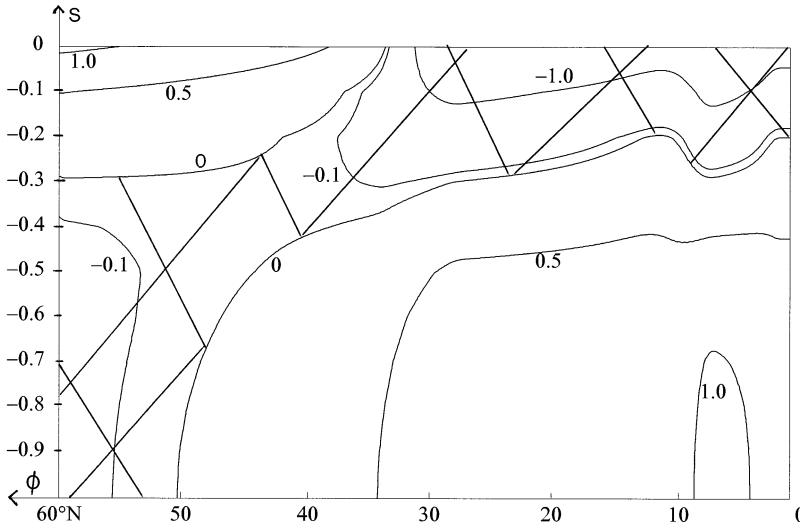


FIG. 18—Distribution of zonal velocity,  $u$ , at the western boundary ( $\lambda = 0$ ). Areas where  $u$  is negative (westward flow) are shaded.

Figure 17 shows the vertical velocity,  $w$ , distribution at the western boundary ( $\lambda = 0$ ) and at the eastern boundary ( $\lambda = \lambda_E$ ) and both exhibit substantial change (outside the equator region) from the zero-order,  $w$ , given by (3.2.3) and shown in Fig. 11 (dashed curves). However, all distributions show similar structure with depth and similar magnitudes for  $w$ .

Figure 18 shows the zonal velocity,  $u$ , at the western boundary ( $\lambda = 0$ ) and shows change (but not significant change in that the magnitudes of  $u$  are similar) from the zero-order  $u$  at  $\lambda = 0$  shown in Fig. 4. Figure 19 shows the zonal velocity,  $u$ , at the eastern boundary ( $\lambda = \lambda_E$ ) and shows change (e.g. slightly decreased magnitudes for  $u$  in the lower ocean) from the zero-order  $u$  at  $\lambda = \lambda_E$  shown in Fig. 5.

## 5 Discussion

The simple model of the abyssal circulation presented here is a generalisation of the Stommel–Arons model by allowing temperature (homogeneous in Stommel–Arons) to vary with depth and latitude and weakly with longitude. The influence of thermal wind in the flow fields is seen to be of major significance, and the resulting flow field for the North Atlantic is significantly different to the Stommel–Arons picture. This flow field for the North Atlantic is consistent with some observations presented in [14] and with some results from the three-dimensional numerical model of the North Atlantic circulation given in [1]. The numerical procedure developed here provides a quite general solution process for the steady planetary geostrophic equations in situations where there is weak zonal variation in temperature (or equivalently density).

Results presented here agree with some results in [9] (for the case of almost-uniform upwelling). A significant characteristic of the model in [9] is that, since

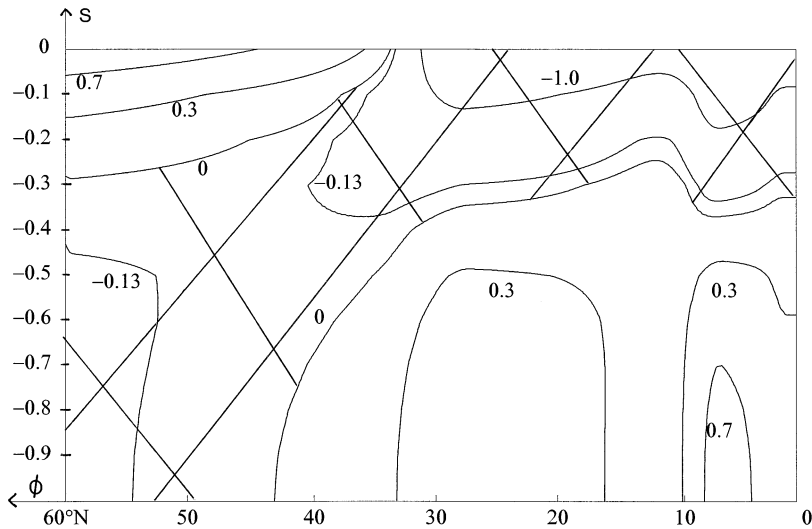


FIG. 19—Distribution of zonal velocity,  $u$ , at the eastern boundary ( $\lambda = \lambda_E$ ). Area where  $u$  is negative is shaded.

upwelling velocity is zero in the western ocean following exponential decrease from its maximum at the eastern boundary, the meridional velocity is forced to change sign with depth (in the western ocean). This alteration in sign (with depth) of the meridional velocity agrees with observations from which it can be deduced that Antarctic Bottom water flows north beneath North Atlantic Deep water flowing south beneath Antarctic Intermediate water flowing north all beneath the thermocline in the western ocean. The model presented here does not exhibit such behaviour in the western ocean since, being a perturbation from zonally invariant upwelling velocity, it is not able to accommodate the necessary large changes in upwelling velocity between the eastern boundary and the western ocean.

A striking feature of the results here is that very small zonal variations in temperature produce very large changes with depth in meridional velocity. This is a dramatic contrast with the depth-invariant meridional velocity which occurs when temperature is zonally invariant. This suggests that models involving the planetary geostrophic equations must allow meridional velocity to vary with depth even when there is very small zonal variation in temperature.

The topography of the ocean basin was neglected here. It is clear that the solution process presented can deal with minor topographic variation in the zonal direction to, for example, model the mid-Atlantic ridge since the inclusion of such topography would introduce only weak zonal variation in the bottom boundary conditions which here are zonally invariant.

In the model presented here there are unresolved boundary layers at both the eastern and western boundaries from which the flow emerges with determined distributions of velocity and temperature. To describe completely both the flow field

and the temperature field it is necessary to resolve these boundary layers where viscosity and horizontal heat diffusion (neglected here) are important.

#### ACKNOWLEDGEMENTS

This work was financially supported by Forbairt Basic Research Grant SC/95/319. The authors wish to thank an anonymous reviewer for helpful comments.

#### REFERENCES

- [1] P.S. Bogden, R.E. Davis and R. Salmon, The North Atlantic circulation: combining simplified dynamics with hydrographic data, *Journal of Marine Research* **51** (1993), 1–52.
- [2] C.A. Edwards and J. Pedlosky, The influence of distributed sources and upwelling on the baroclinic structure of the abyssal circulation, *Journal of Physical Oceanography* **25** (1995), 2259–84.
- [3] A.E. Gill, An explicit solution of the linear thermocline equations, *Tellus* **37A** (1985), 276–85.
- [4] P.F. Hodnett and R. McNamara, A modified Stommel–Arons model of the abyssal ocean circulation, *Mathematical Proceedings of the Royal Irish Academy* **100A**(1) (2000), 85–104.
- [5] R.X. Huang, A two-level model for the wind- and buoyancy-forced circulation, *Journal of Physical Oceanography* **23** (1993), 104–15.
- [6] S. Levitus, *Climatological atlas of the world ocean*, NOAA Technical Paper 13, National Oceanic and Atmospheric Administration, Rockville, Md, 1982.
- [7] P.S. Lineykin, On the dynamics of the baroclinic layer in the ocean, *Doklady Akademii Nauk USSR* **117** (1957), 971–4.
- [8] J. Pedlosky, Linear theory of the circulation of a stratified ocean, *Journal of Fluid Mechanics* **16** (1969), 185–205.
- [9] J. Pedlosky, The baroclinic structure of the abyssal circulation, *Journal of Physical Oceanography* **22** (1992), 652–9.
- [10] R. Salmon, A simplified linear ocean circulation theory, *Journal of Marine Research* **44** (1986), 695–711.
- [11] H. Stommel, The abyssal circulation, *Deep-Sea Research* **5** (1958), 80–2.
- [12] H. Stommel and A.B. Arons, On the abyssal circulation of the world ocean—I. Stationary planetary flow patterns on a sphere, *Deep-Sea Research* **6** (1960), 140–54.
- [13] H. Stommel and A.B. Arons, On the abyssal circulation of the world ocean—II. An idealized model of the circulation pattern and amplitude in oceanic basins, *Deep-Sea Research* **6** (1960), 217–33.
- [14] L.V. Worthington and W.R. Wright, *North Atlantic Ocean Atlas*, Woods Hole Oceanographic Institution, Mass., 1970.
- [15] G. Wüst, Schichtung und Zirkulation des Atlantischen Ozeans. Die Stratosphere, in *Wissenschaftliche Ergebnisse der Deutschen Atlantischen Expedition auf dem Forschungs- und Vermessungsschiff 'Meteor' 1925–1927*, vol. 6, parts 1 and 2, Walter de Gruyter, Berlin and Leipzig, 1935.
- [16] Y. Yuan, P.F. Hodnett and J.M. Huthnance, Simulated influence of an eastern boundary slope current on a zonally uniform ocean model, *OMEX Final Report* [CD-ROM], Brussels, 1996.

#### APPENDIX A

The perturbation presented here to the zero-order approximation derived in section 3 is based on the assumption that there is weak zonal variation in the prescribed surface temperature as given by expression (4.1.1), i.e.  $0 < \epsilon \ll 1$ . The perturbed solution is calculated as follows.

##### Step 1

Subdivide  $0 \leq \lambda \leq \lambda_E$  into  $N$  equal divisions, i.e.  $0 = \lambda_0 < \lambda_1 < \lambda_2 < \dots < \lambda_N = \lambda_E$ . We solved for cases  $N = 13$  (with 140 steps in the  $\phi$  direction and 100 steps in the

$s$  direction) and  $N = 23$  (with 70 steps in the  $\phi$  direction and 100 steps in the  $s$  direction), with both cases showing indistinguishable results. The results given are for  $N = 13$  (i.e. subdivisions of approximately  $4^\circ$  in longitude) with 140 steps in  $\phi$  and 100 steps in  $s$ . At fixed  $\lambda = \lambda_i$  (for each  $i = 0, 1, 2, \dots, N$ ) solve the two-dimensional equation

$$w_0 \frac{\partial T}{\partial s} + \gamma v_0 \frac{\partial T}{\partial \phi} = \bar{\beta} \frac{\partial^2 T}{\partial s^2} \quad (\text{A.1})$$

using the method described in section 3 and with  $v_0, w_0$  as given in (3.2.2) and (3.2.3), and subject to the same boundary conditions as in section 3 except that

$$T|_{s=0} \equiv T_s(\lambda_i, \phi) = \left[ T_s(\phi) + \epsilon \frac{\lambda_i}{\lambda_E} \sin^3 3\phi \right]. \quad (\text{A.2})$$

This gives a first approximation to  $T$  (at each station  $\lambda_i$ ) which is denoted by  $T_1(\lambda_i, \phi, s)$ .

### Step 2

Determine  $\partial T_1 / \partial \phi$  and  $\partial T_1 / \partial \lambda$  by the central differences

$$\frac{\partial T_1(\lambda_i, \phi_j, s)}{\partial \phi} = \frac{T_1(\lambda_i, \phi_{j+1}, s) - T_1(\lambda_i, \phi_{j-1}, s)}{2\Delta\phi} \quad (\text{A.3})$$

$$\frac{\partial T_1(\lambda_i, \phi_j, s)}{\partial \lambda} = \frac{T_1(\lambda_{i+1}, \phi_j, s) - T_1(\lambda_{i-1}, \phi_j, s)}{2\Delta\lambda} \quad (\text{A.4})$$

where  $\Delta\phi = \phi_j - \phi_{j-1}$  and  $\Delta\lambda = \lambda_i - \lambda_{i-1}$ . The expressions (2.8), (2.9) and (2.10) then give the first approximations to  $v, w, u$  (at each station  $\lambda_i$ ) which we denote by  $v_1(\lambda_i, \phi, s), w_1(\lambda_i, \phi, s)$  and  $u_1(\lambda_i, \phi, s)$  respectively.

### Step 3

At fixed  $\lambda = \lambda_i$  (for each  $i = 0, 1, 2, \dots, N$ ) solve iteratively the equation

$$\bar{w}_k(\lambda_i, \phi, s) \frac{\partial T}{\partial s} + \gamma \bar{v}_k(\lambda_i, \phi, s) \frac{\partial T}{\partial \phi} + \gamma \frac{\bar{u}_k(\lambda_i, \phi, s)}{\cos \phi} \frac{\partial T_k}{\partial \lambda} = \bar{\beta} \frac{\partial^2 T}{\partial s^2}, \quad (\text{A.5})$$

subject to the same boundary conditions as before for  $k = 1, 2, 3, \dots$  where

$$\bar{w}_k(\lambda_i, \phi, s) = \frac{1}{2} [w_{k-1}(\lambda_i, \phi, s) + w_k(\lambda_i, \phi, s)], \quad (\text{A.6})$$

$$\bar{v}_k(\lambda_i, \phi, s) = \frac{1}{2} [v_{k-1}(\lambda_i, \phi, s) + v_k(\lambda_i, \phi, s)], \quad (\text{A.7})$$

$$\bar{u}_k(\lambda_i, \phi, s) = \bar{\alpha}_k u_k(\lambda_i, \phi, s), \quad (\text{A.8})$$

where  $\bar{\alpha}_k$  is a relaxation factor (discussed later) and  $T_k, w_{k-1}, w_k, v_{k-1}, v_k, u_k$  were determined at the previous iteration. This gives the  $(k+1)$  approximation to  $T$  (at each station  $\lambda_i$ ), i.e.  $T_{k+1}(\lambda_i, \phi, s)$  for  $i = 0, 1, 2, \dots, N$ . Expressions (2.8), (2.9), (2.10) are then used to determine  $v_{k+1}, w_{k+1}, u_{k+1}$  respectively.

*Step 4*

Calculate  $Er = \max |T_{k+1}(\lambda_i, \phi, s) - T_k(\lambda_i, \phi, s)|$ . If  $Er < \delta$  (see later for value), then the process is complete and the solution is

$$\begin{aligned} T(\lambda_i, \phi, s) &= T_{k+1}(\lambda_i, \phi, s) \\ v(\lambda_i, \phi, s) &= v_{k+1}(\lambda_i, \phi, s) \\ w(\lambda_i, \phi, s) &= w_{k+1}(\lambda_i, \phi, s) \\ u(\lambda_i, \phi, s) &= u_{k+1}(\lambda_i, \phi, s). \end{aligned}$$

Otherwise return to Step 3.

Since the convergence to a solution of numerical iteration schemes is adversely affected by large changes in values of variables between iteration steps, we introduced the following relaxation processes to prevent this happening. We used the average  $\bar{w}_k$  of previous values  $w_{k-1}$  and  $w_k$  (as given in (A.6)) and similarly  $\bar{v}_k$  (as given in (A.7)) in the solution of equation (A.5). We used the relaxation factor  $\bar{\alpha}_k$  occurring in (A.8) in the following way. To ensure that the influence of the  $\bar{u}_k$  term in equation (A.5) is small at the first step  $k = 1$  we set  $\bar{\alpha}_1 = 0.5$  and for the remaining steps  $\bar{\alpha}_k = 1.0$  (for  $k \geq 2$ ). The maximum value of the small error  $\delta = 0.048$  (for the results reported here) occurred at

$$\lambda = \frac{5}{6}\lambda_E, \quad \phi = 44^\circ \text{ N}, \quad s = -1/3.$$